https://doi.org/10.5194/egusphere-2026-3261
Preprint. Discussion started: 7 July 2026

Ozone Downward Flux Revealed by High-Resolution Differential Absorption Lidar over Tibet during Stratosphere-Troposphere Exchange

Ruichun Dong[1], Xin Fang[1,2], Chengyun Yang[1,2], Tao Li[1,2]

[1]National Key Laboratory of Deep Space Exploration/School of Earth and Space Sciences, University of Science and Technology of China, Hefei, Anhui, China
[2]CAS Center for Excellence in Comparative Planetology/CAS Key Laboratory of Geospace Environment/Mengcheng National Geophysical Observatory, University of Science and Technology of China, Hefei, Anhui, China

Correspondence to: Xin Fang (xinf@ustc.edu.cn)

Abstract. This study characterizes a prominent ozone intrusion event driven by stratosphere-to-troposphere exchange (STE) that occurred on 18-19 October 2017. The analysis is enabled by high spatiotemporal resolution ozone profile observations from the USTC Ozone Lidar deployed at Yangbajing, Tibet (29°N, 99°E). It provides the first lidar-based detection of these rapid ozone descent events and the evidence linking them to temperature variability in the tropopause region through lidar-derived temperature profiles, revealing temperature gradients that generally exceed 8 K km^{-1} during these events and beyond the resolving capability of conventional atmospheric model products. Combining Wei's flux diagnostic with a sensitivity test of PV-based dynamical tropopause thresholds identifies 3 PVU as the most suitable definition for this case. ECMWF Reanalysis v5 (ERA5) is then used to characterize the spatiotemporal evolution of cross-tropopause mass fluxes over 25-28°N, 95-99°E, showing that the ozone variations observed by the lidar were modulated by gravity waves associated with the tropopause fold. In addition, lidar-measured ozone profiles are incorporated into a cross-tropopause ozone flux calculation framework, yielding an instantaneous peak STE ozone flux of about $3\sim4\cdot10^{-10}\cdot kg\cdot s^{-1}\cdot m^{-2}$, slightly higher than the corresponding ERA5 value, while maintaining strong agreement in overall flux magnitude and temporal evolution throughout the event. These results show that high-resolution vertical ozone observations and Raman-retrieved temperature profiles from the USTC Ozone Lidar, combined with wind field data, enable accurate quantification of STE-related ozone fluxes. This approach facilitates in-depth investigation of coupled atmospheric composition and dynamical processes.

1 Introduction

Stratosphere-Troposphere Exchange is one of the key mechanisms controlling the budgets of ozone, water vapor, and other trace constituents in the upper troposphere and lower stratosphere (UTLS) region (Chen et al., 2006). Lelieveld argued that STE exerts a strong influence on upper-tropospheric ozone and plays an important role in the UTLS radiative budget, dynamical structure, chemical processing, and microphysical evolution (Lelieveld et al., 2000). At the global scale, exchange between the stratosphere and troposphere exhibits pronounced regional contrasts. Shaped by the distinctive topography and

https://doi.org/10.5194/egusphere-2026-3261
Preprint. Discussion started: 7 July 2026

circulation systems, the Tibetan Plateau and its surrounding regions display unique patterns of atmospheric composition and dynamical structure, imparting strong regional characteristics to STE. As a result, this high-elevation domain serves as a key corridor and observational window for energy and mass fluxes between the stratosphere and troposphere, with important implications for understanding coupled atmospheric processes on the global scale (Yang et al., 2004; Chen et al., 2010).

Given that STE is a major physical mechanism governing the distribution and variability of atmospheric trace constituents in the UTLS, extensive observational and modeling studies have been devoted to this process, with particular attention to ozone over the Tibetan Plateau and the mechanisms shaping its distribution. For example, Zhou used TOMS satellite data to identify a summertime minimum in total column ozone over the Plateau, referred to as the ozone valley, and linked it to ascent over the mountainous terrain (Zhou et al., 2005). Subsequent work further showed that both thermodynamic and dynamical forcing over the Plateau make important contributions to the formation and maintenance of this ozone minimum (Randel et al., 2006; Randel et al., 2010). Using TOMS satellite observations together with chemistry-climate model simulations, Tian et al (Tian et al., 2008) found that the overall uplift of the summertime tropopause over the Plateau alters the vertical ozone distribution, leading to a systematic reorganization of ozone stratification within the UTLS. In addition, based on case analyses of ozonesonde profiles on the northeastern flank of the Plateau, Chen et al (Chen et al., 2012) reported clear signatures of stratospheric air intruding into the troposphere along the periphery of a strong upper-tropospheric anticyclone, directly illustrating how STE modulates regional ozone distributions. Together, these findings indicate that the distinctive composition and dynamics over Tibet endow STE-related downward ozone transport with pronounced regional characteristics, while also placing the region in a pivotal position for understanding Stratosphere-Troposphere Exchange on the global scale.

Using a springtime case study of a tropopause-folding event, Zhang demonstrated that an upper-level jet associated with the intrusion of a low-pressure trough over the Tibetan Plateau was the primary dynamical driver (Zhang et al., 2010). During the subsequent evolution, both troposphere-to-stratosphere transport (TST) and stratosphere-to-troposphere transport (STT) occurred, indicating a complex, bidirectional exchange. However, the scarcity of high-spatiotemporal-resolution observations over the Plateau has hindered a systematic characterization of the fine structure of stratospheric intrusions into the troposphere and their specific impacts on the vertical distribution of ozone. For decades, the paucity of high-resolution observations over Tibet has severely constrained systematic investigations of STE-driven downward ozone transport, and of the accompanying evolution of atmospheric chemical constituents and dynamical processes. To fill this observational gap, we developed a mobile differential absorption lidar (DIAL) system (Fang et al., 2019) capable of high-resolution, long-duration, continuous profiling of ozone in both the troposphere and the stratosphere.

Based on measurements from this platform, we present a comprehensive analysis of an STE-related ozone descent event over Tibet. Section 2 describes the datasets used in this study, with emphasis on the mobile differential absorption ozone lidar deployed at Yangbajing, Tibet, and presents intercomparisons and accuracy validation of the retrieved ozone profiles. In Section 3, we corroborate the STE-related ozone descent detected by the lidar using ERA5 global reanalysis fields; we then select an appropriate tropopause definition and diagnose cross-tropopause mass fluxes over the observational domain, quantifying the spatial distribution of the mass flux across the tropopause. Building on these diagnostics, we combine the lidar-

https://doi.org/10.5194/egusphere-2026-3261
Preprint. Discussion started: 7 July 2026

measured ozone profiles with ERA5 wind fields to estimate cross-tropopause ozone fluxes, enabling a quantitative, observation-based assessment. Section 4 summarizes the main conclusions and outlines directions for future work.

2 Data sources and lidar system overview

The data used in this study were acquired with a mobile differential absorption lidar (USTC Ozone Lidar) system deployed by our group at Yangbajing, Tibet (29°N, 99°E), which enables simultaneous observations of ozone in both the troposphere and stratosphere. Satellite imagery of the lidar site in Tibet and the on-site layout of the ozone lidar system are shown in Fig. 1(a-b), respectively. After performance tuning and testing in Huainan, Anhui Province, the mobile ozone lidar system was transferred to Yangbajing for routine observations beginning in October 2017. It is one of the few mobile DIAL stations worldwide capable of simultaneously profiling tropospheric and stratospheric ozone (McDermid et al., 1991; Godin-Beekmann et al., 2003; Hansen et al., 2003; Baray et al., 2013), and represents a distinctive example of such a system operating at the highest altitude among comparable platforms globally (~4,300 m above sea level).

The mobile differential absorption ozone lidar combines the differential absorption technique with distinct backscattering mechanisms. Schematics of the mobile ozone DIAL system and of the emission reception configuration for the different detection wavelengths are shown in Fig. 1(c) and 1(d), respectively. For tropospheric ozone measurements, the system emits a differential absorption wavelength pair at 289 and 299 nm, and receives the corresponding tropospheric Mie/Rayleigh backscattered signals. For stratospheric ozone measurements, it emits a second differential absorption pair at 308 and 355 nm, and detects the corresponding Rayleigh backscatter signals from the upper stratosphere. In parallel, the system also records Raman backscatter signals at 332 and 387 nm, corresponding to N_2 Raman-shifted returns from 308 and 355 nm, respectively, over the upper troposphere and middle stratosphere, thereby reducing the influence of aerosol backscatter. In the receiver subsystem, four independent telescopes, each with a 1.25 m aperture, are combined into a collecting array with an effective diameter exceeding 2.2 m to detect signals at 308, 332, 355, and 387 nm, enabling ozone measurements from the tropopause to the upper stratosphere over an altitude range of 18-50 km. This array-based design enhances the signal-to-noise ratio for stratospheric observations. A separate 1 m aperture prime-focus telescope receives the 289 and 299 nm signals for ozone detection over 8-19 km, while two 0.21 m aperture Newtonian telescopes receive the same wavelengths for measurements over 5-10 km, thereby extending coverage from the troposphere to the lower stratosphere across 5-19 km. Together, the seven telescopes provide simultaneous ozone profiling from 5 to 50 km, spanning both the troposphere and stratosphere.

https://doi.org/10.5194/egusphere-2026-3261
Preprint. Discussion started: 7 July 2026

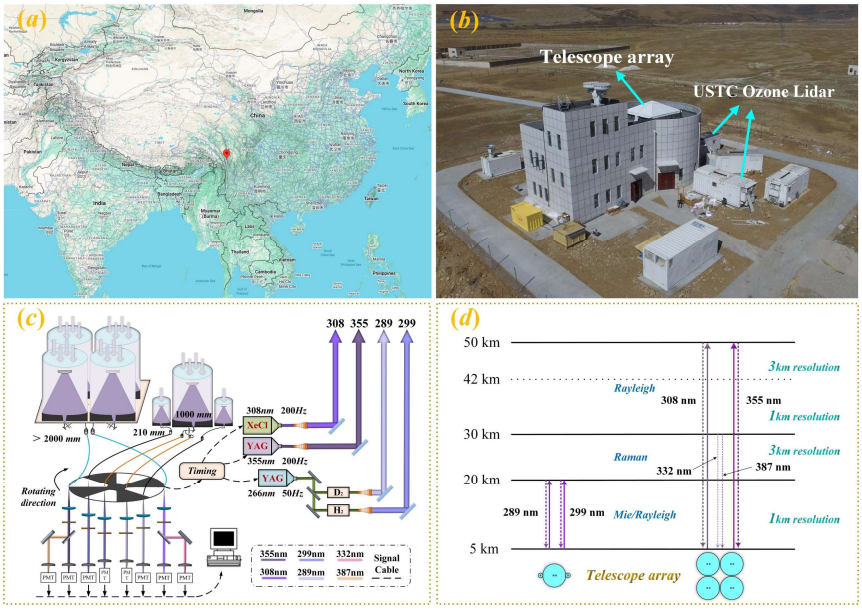

Figure 1: (a) Satellite image of the radar observation site on the Tibetan Plateau (Map data © Google Earth 2026); (b) Field layout of the ozone lidar system; (c) Schematic of the mobile ozone lidar system; (d) Altitude ranges corresponding to different laser emission wavelengths.

To ensure accurate ozone measurements, the laser beam axis must be properly aligned with the receiving telescope, and the telescope field of view must adequately overlap with the laser emission field. As shown in Fig. 1(c), a mechanical chopper was placed in the optical path to reduce noise from strong near-field backscatter. In routine operation, the system records a raw signal file every minute, with a vertical bin size of 61.44 m and 2,048 range bins. To ensure adequate signal quality in the stratosphere, photon-counting returns are accumulated over 30 min and corrected for saturation, yielding the wavelength-dependent photon profiles and signal-to-noise ratios (SNR) shown in Fig. 2(a-d). As shown in Fig. 2, the SNR is sufficient across the altitude ranges corresponding to the different wavelengths presented in Fig. 1(c-d).

https://doi.org/10.5194/egusphere-2026-3261
Preprint. Discussion started: 7 July 2026

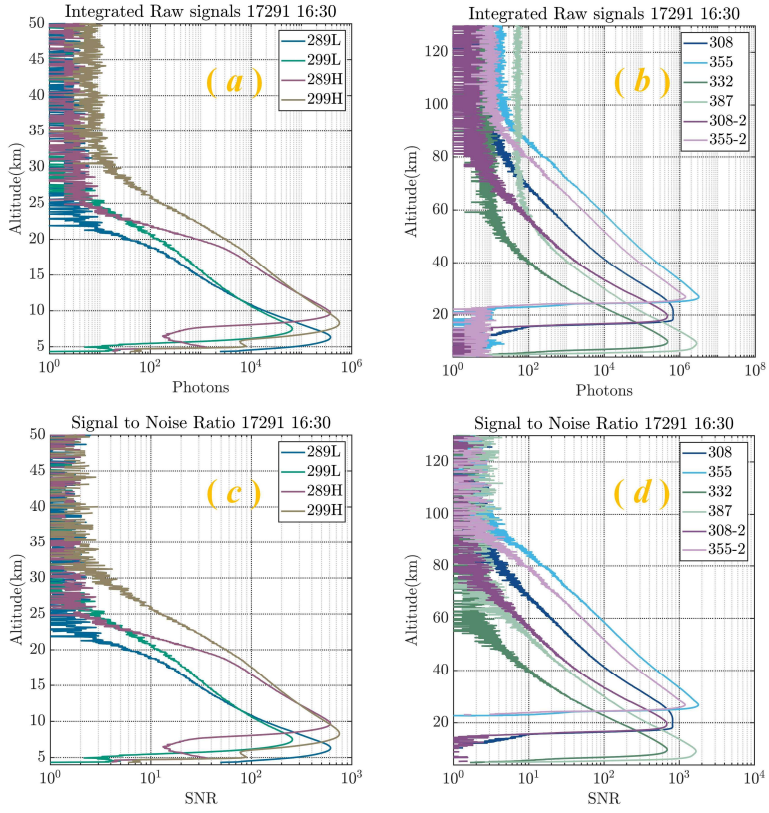

Figure 2: Wavelength-dependent photon returns and corresponding signal-to-noise ratios for the mobile ozone DIAL system (USTC Ozone Lidar).

Background noise, averaged over the altitude range 115-125 km, was subtracted from the raw signals. After denoising the raw backscattered optical signals using wavelet-transform-based signal processing (Fang et al., 2004; Yin et al., 2006; Boggess et al., 2009), ozone concentrations at different detection wavelengths and altitudes were retrieved using the differential absorption lidar equation (Kovalev et al., 2004). In the retrieval, we accounted comprehensively for the key factors affecting the solution of the equation, including the temperature dependence of the absorption cross-sections, absorption by other trace gases within the operating spectral range, and the backscatter term (Weitkamp et al., 2005).

The ozone number density profiles retrieved from the lidar observations over five altitude intervals are shown in Fig. 3(a). Because differences in detection wavelength, laser pulse energy, and telescope field of view determine the effective retrieval range for each channel, the five profile segments were merged using 3-bin overlap regions to produce a continuous ozone profile. The merged profile was then compared with ERA5 data at the corresponding time, and further cross-validated against

https://doi.org/10.5194/egusphere-2026-3261
Preprint. Discussion started: 7 July 2026

observations from the Ozone Monitoring Instrument (OMI) and the Microwave Limb Sounder (MLS) aboard the Aura satellite, as shown in Fig. 3(b).

The results show that the ozone profile retrieved from USTC Ozone Lidar agrees well overall with ERA5. It should be noted, however, that satellite observations are constrained by orbital sampling and overpass timing. On this day, the MLS overpass occurred at 18:50 UT at 25.22°N, 105.20°E. Below 25 km, the observed ozone concentrations were broadly consistent with the USTC Ozone Lidar measurements, whereas above 25 km, MLS showed systematically higher ozone concentrations at the same altitudes. This discrepancy is likely related to the large spatial separation between the satellite overpass location and the lidar site. By contrast, the OMI overpass occurred at 07:10 UT at 27.07°N, 99.34°E. Above 25 km, the ozone concentrations agreed well with the USTC Ozone Lidar retrievals, whereas below 25 km, OMI exhibited a certain positive bias relative to the lidar measurements. Although the spatial distance between the satellite footprint and the lidar station was minimized, the relatively long temporal separation between the OMI overpass and the lidar observations at the same location may still have introduced appreciable differences in ozone concentration. Overall, USTC Ozone Lidar shows good consistency with ERA5, and the two datasets provide robust, complementary constraints. Moreover, the high spatial and temporal resolution of the lidar allows it to resolve fine-scale structures that are often missed by other datasets, since satellite profile data typically contain only about a dozen vertical points and ERA5 records only slightly more than 30 levels. This capability is particularly valuable for detecting and analyzing short-lived but dynamically intense cross-tropopause ozone transport events.

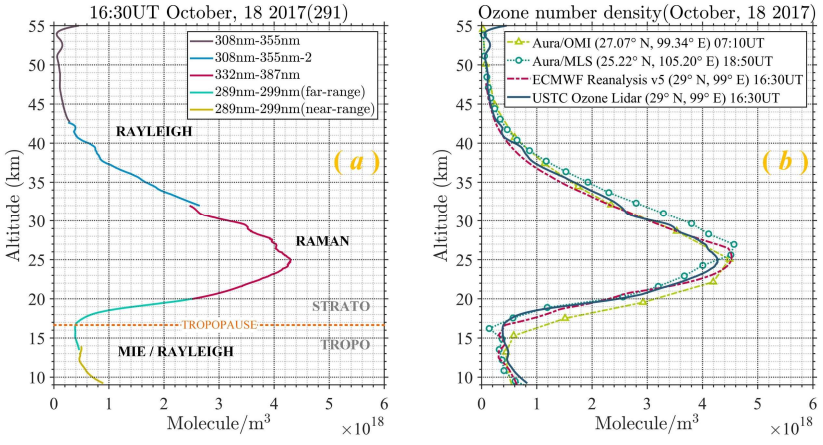

Figure 3: (a) Retrieved ozone concentration profiles from the ozone lidar over different altitude ranges; (b) Comparison of the merged ozone profile with ERA5 reanalysis and Aura/OMI and Aura/MLS satellite observations.

https://doi.org/10.5194/egusphere-2026-3261
Preprint. Discussion started: 7 July 2026

3 Methods and Results

3.1 Lidar observations and supporting evidence for a STE-related ozone descent event

The USTC Ozone Lidar deployed at Yangbajing, Tibet (29°N, 99°E) was developed in-house by the University of Science and Technology of China. The system enables simultaneous profiling of ozone in the troposphere and stratosphere with high spatial and temporal resolution, providing a particularly valuable observational constraint on ozone variability over the Tibetan Plateau, where in situ data remain sparse. The lidar retrievals also allow us to identify clear signatures of downward ozone transport. Influenced by its unique high elevation topography and the Asian monsoon, the Tibetan Plateau is recognized as one of the most active regions for Stratosphere-Troposphere Exchange (STE) (Chen et al., 2006). Under these conditions, ozone transport from the stratosphere across the tropopause is likely to be an important source of background tropospheric ozone over Tibet, with potential implications for regional climate regulation and for the global coupling of chemistry and climate (Gettelman et al., 2002; Duan et al., 2005). In this section, we use ERA5 global reanalysis fields (0.25° × 0.25° spatial resolution; 1 h temporal resolution) as supporting evidence to analyze the STE event captured by the ozone-profiling lidar and to provide an initial observational assessment of its evolution.

As shown in Fig. 4, USTC Ozone Lidar captures the temporal evolution of ozone concentration near the tropopause above Yangbajing, based on observations acquired during the nights of 18 and 19 October 2017. To ensure an adequate signal-to-noise ratio, photon-counting returns were accumulated over 30 mins and processed using a moving time-window method (Duchnowski et al., 2025), yielding a continuous ozone concentration distribution as a function of height and time. It is worth noting that ozone DIAL measurements are conducted only at night and are limited by weather conditions. As a result, the ozone results typically appear as banded segments separated by temporal gaps, shown in Fig. 4. Figure 4(a) shows the ozone descent observed by USTC Ozone Lidar over Yangbajing during 16:00-21:00 on 18 October. The lidar retrievals reveal a pronounced downward extension of an ozone-enhanced layer, appearing as a tilted, downward-evolving structure in the time-height cross section (blue arrow in Fig. 4(a)). Figure 4(b) presents the subsequent recovery phase observed during 15:00-21:00 on 19 October. The retrievals indicate a clear rebound signal, with the ozone-enhanced structure evolving with an overall upward tilt in the time–height cross-section (orange arrow in Fig. 4(b)).

https://doi.org/10.5194/egusphere-2026-3261
Preprint. Discussion started: 7 July 2026

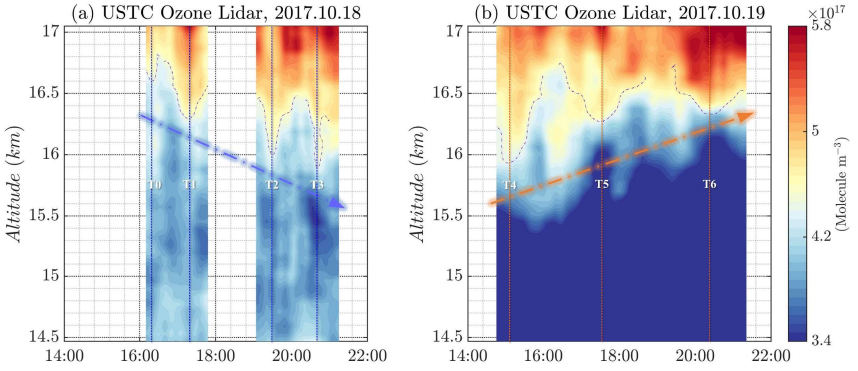

Figure 4: (a) Downward ozone transport observed by USTC Ozone Lidar on 18 October 2017; (b) Recovery phase following the ozone descent observed by USTC Ozone Lidar on 19 October 2017.

A notable feature of the retrieval results is that the lidar resolved numerous episodes of rapid downward ozone transport on short time scales (as shown by T0-T6 in Fig. 4). Some events lasted one to two hours, while others persisted for less than one hour. These short-lived transient features are unlikely to be represented in satellite observations or in some atmospheric model datasets. Previous studies have given limited attention to such events. Their repeated occurrence suggests that they may offer a valuable perspective on STE processes beyond that provided by events analyzed over longer time scales.

To corroborate the suspected STE-related ozone descent observed by the ozone lidar in autumn 2017, we further use ERA5 global reanalysis fields as an independent line of evidence. A prerequisite for diagnosing cross-tropopause exchange during STE events is a robust identification of the tropopause. For an initial ERA5-based screening of the event, the tropopause height is determined using the thermodynamic definition. Following the World Meteorological Organization (WMO) lapse-rate criterion proposed in 1986 (Wei et al., 1987), the thermodynamic tropopause is defined as the lowest level above the 500 hPa surface at which the atmospheric temperature lapse rate decreases to 2 °C km^{-1} or less, provided that the mean lapse rate within the 2 km layer above this level does not exceed 2 °C km^{-1}. Based on this criterion, the tropopause position can be readily identified from ERA5 gridded fields. Analysis of ERA5 data during the periods covered by USTC Ozone Lidar observations reveals a pronounced cross-tropopause ozone descent event. We therefore focus on ERA5 data at the Yangbajing site for 16-19 October 2017. The continuous temporal coverage provided by ERA5 during this period allows the evolution of the event to be captured more completely, as illustrated in Fig. 5(a). A strong STE-related ozone descent is evident during 18-19 October 2017, in close agreement with the USTC Ozone Lidar observations.

https://doi.org/10.5194/egusphere-2026-3261
Preprint. Discussion started: 7 July 2026

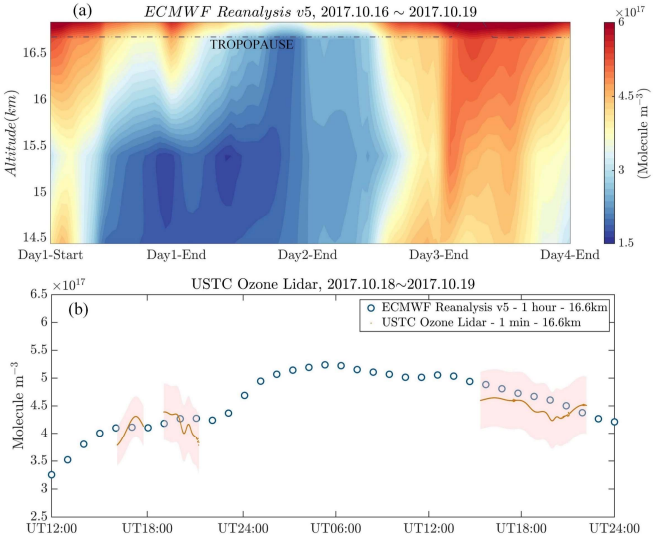

Figure 5: (a) ERA5 depiction of the STE evolution near the tropopause over Yangbajing during 16–19 October 2017; (b) Comparison of lidar-observed and ERA5 ozone concentrations at the tropopause level (16.6 km) during 18-19 October 2017.

Both the USTC Ozone Lidar observations and ERA5 capture the onset and recovery phases of this ozone descent event. Differences between the lidar-retrieved ozone concentrations and those from ERA5 are further quantified. As shown in Fig. 5(b), the ozone number density variations observed by the USTC Ozone Lidar during the STE event are compared with the corresponding ERA5 values. To ensure a consistent comparison, the analysis is performed at the tropopause level (16.6 km), and the 95% confidence interval of the lidar retrievals is also shown. Notably, ERA5 provides hourly-resolution data, whereas the ozone lidar yields full-profile ozone measurements with 1-min update intervals. Figure 5(b) shows that the tropopause-level (16.6 km) ozone number densities measured by the USTC Ozone Lidar during 18-19 October 2017 agree closely with ERA5 in both absolute magnitude and temporal evolution. However, comparing Fig. 5(a) with Fig. 4(b) indicates that during the recovery phase on 19 October 2017, the ozone number densities retrieved by USTC Ozone Lidar below 15.5 km are systematically slightly lower than those in ERA5. Given the high SNR of the lidar returns during this period, the discrepancy is more likely to reflect a modest overestimation by ERA5 of the ozone number density associated with stratosphere-to-troposphere transport at this stage.

3.2 Tropopause definition and cross-tropopause flux diagnostics

Mass and trace-constituent exchange between the stratosphere and troposphere is a central component of the coupled troposphere–stratosphere system. In 1987, Wei proposed a diagnostic framework for quantifying this exchange, in which all

https://doi.org/10.5194/egusphere-2026-3261
Preprint. Discussion started: 7 July 2026

physical processes contributing to cross-tropopause transport can be expressed in an explicit mathematical form (Reiter., 1975; Wirth et al., 1999). The general form can be written as:

$$F(f) = [\rho J_\eta f \left(\frac{d\eta}{dt} - \frac{\partial \eta}{\partial t_{z_0}} - \vec{\mathrm{U}} \cdot \nabla_{z_0} \eta\right)]_{\eta_B} , \quad (1)$$

where $F(f)$ is the air mass flux across the tropopause, ρ is the air density near the tropopause, η is a generalized vertical coordinate, $J_\eta = \partial z/\partial \eta$ is the Jacobian of the coordinate transformation, z_0 denotes the tropopause, $d\eta/dt$ is the vertical velocity in η coordinates, $\vec{\mathrm{U}}$ is the horizontal wind vector, and f is the constituent mixing ratio. In pressure coordinates, this expression becomes:

$$F(\rho) = -g^{-1}\left(w - \vec{\mathrm{U}} \cdot \nabla_{z_0} p - \frac{\partial p}{\partial t_{z_0}}\right), \quad (2)$$

A key advantage of Wei's diagnostic formulation is that it allows the upward and downward cross-boundary fluxes to be computed separately and can be applied to any atmospheric constituent across an arbitrary reference surface. Given the large contrast in ozone mass mixing ratios between the stratosphere and troposphere, and the common assumption that an air mass becomes well mixed over a relatively short timescale after crossing the tropopause, quantitative assessments based on ozone profiles require the upward and downward fluxes to be treated separately. As noted above, we initially located the thermodynamic tropopause using changes in the vertical temperature lapse rate. In some situations, however, particularly near jet streams, this tropopause can be poorly defined. Because the following analysis examines lidar observations in detail and because the Yangbajing site lies in the low-to-mid latitudes, where large-scale dynamics and strong disturbances can substantially perturb the thermal structure, defining the tropopause solely from lapse-rate criteria may introduce appreciable uncertainty. Holton noted that the tropopause is better regarded as a quasi-material surface (Holton et al., 1995). This perspective is well captured by the dynamical tropopause defined in terms of potential vorticity (PV), and cross-tropopause transport studies therefore commonly adopt a PV-based tropopause, typically using thresholds in the range of 1.5-4 PVU (where PVU denotes the potential vorticity unit). Moreover, Yang et al showed that the choice of PV threshold can substantially affect estimates of cross-tropopause exchange, and advocated selecting an optimal threshold based on its correlation with observations or diagnostic quantities (Yang et al., 2003).

Following the approach of Yang et al, we conduct a sensitivity analysis over a domain centered on the Yangbajing ozone lidar site (29°N, 99°E), spanning 25-32°N and 94-104°E, to assess how the choice of PV threshold influences the diagnosed cross-tropopause flux. As shown in Fig. 6, we quantify the changes in cross-tropopause transport on 18-19 October 2017 associated with different PV thresholds within this region. The results indicate that the estimated cross-tropopause flux is highly sensitive to the choice of threshold. For PV thresholds below 3 PVU, both upward and downward transports are relatively large, exhibiting more tropospheric characteristics; for thresholds above 3 PVU, both transports are markedly smaller, consistent with more stratospheric behavior. With increasing PV threshold, the total exchange in both troposphere-to-stratosphere transport (TST) and stratosphere-to-troposphere transport (STT) decreases. In addition, the magnitudes and temporal evolution

https://doi.org/10.5194/egusphere-2026-3261
Preprint. Discussion started: 7 July 2026

of TST and STT suggest that, before and after the onset and recovery of the descent event on 18-19 October 2017, the total cross-tropopause transport over the study region is broadly consistent with mass conservation.

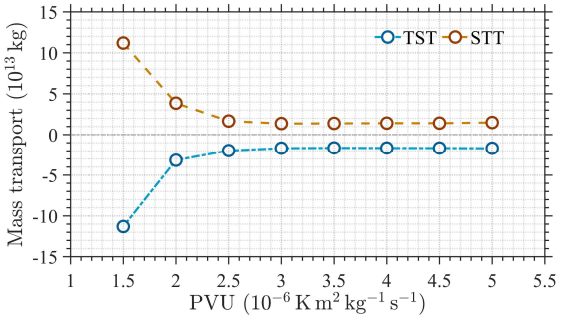

Figure 6: Transport sensitivity to PVU threshold during 18-19 October 2017.

Furthermore, as shown in Fig. 7(a-b), to ensure spatial continuity and robustness of the tropopause definition, we construct two PVU cross-sections from ERA5 in the vicinity of the lidar site: a zonal section along 90-110°E and a meridional section along 24-34°N. These sections show that, in some areas, tropopauses defined using lower PVU thresholds become discontinuous in pressure coordinates. By contrast, the continuity and stability improve markedly for thresholds of 2 PVU and above. Combining the sensitivity results with the cross-section structures, we consider 3 PVU (1 PVU = 10^{-6}·m^2·s^{-1}·kg^{-1}) to be a reasonable dynamical tropopause threshold for this event (highlighted with an orange line in fig.7(a-b)).

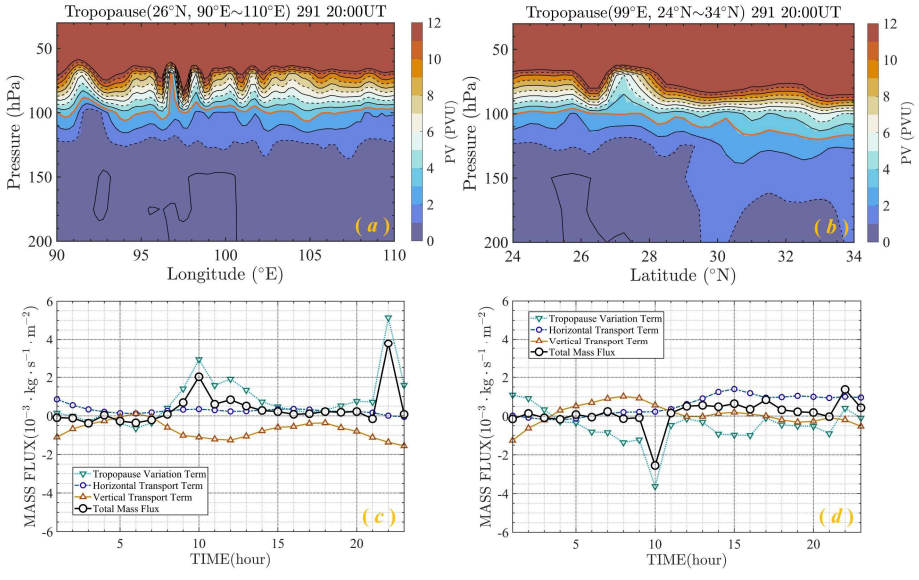

https://doi.org/10.5194/egusphere-2026-3261
Preprint. Discussion started: 7 July 2026

Figure 7: (a) Zonal potential vorticity cross-section over the Tibetan Plateau region; (b) Meridional potential vorticity cross-section over the Tibetan Plateau region; (c) Time evolution of the domain-mean transport components on 18 October; (d) Time evolution of the domain-mean transport components on 19 October.

Fig. 7(c-d) shows the time evolution of the domain mean transport components over 18-19 October 2017, diagnosed from ERA5. The vertical wind contribution remains relatively steady over the two days. The horizontal wind contribution is of comparable magnitude but opposite sign, so that the net flux is controlled to a large extent by variations in the tropopause. It should be stressed that tropopause undulations mainly modify the geometric boundary used in the flux diagnosis and do not, by themselves, generate strong and persistent local transport.

Given the observed tropopause variations, a natural question is whether they were driven by temperature fluctuations in the tropopause region, and in particular whether such temperature changes corresponded to the short-lived, rapid ozone descent events shown in Fig. 4. ERA5, however, does not provide temperature profiles with sufficient temporal resolution to address this question, as its output is available only at hourly intervals. As described in Section 2, the USTC Ozone Lidar also recorded the N_2 vibrational Raman backscatter signals at 332 and 387 nm, corresponding to the 308 and 355 nm emission wavelengths, respectively, and these signals exhibit sufficient signal-to-noise ratio over the 14 to 30 km altitude range, as shown in Fig. 8(a). Because 332 nm remains within the ozone absorption band, the 387 nm Raman signal was used to retrieve the temperature profiles. The retrieval, shown in Fig. 8(b), used the USSA1976 model at 50 km as the reference and proceeded downward to derive the temperature structure. Comparison with ERA5 at the same times shows that the two temperature profiles are in close agreement. Figure 8(c-d) present the temperature variations retrieved from the 387 nm return over 14.5 to 17 km, where the temperature enhancements at the seven times T0 to T6 correspond closely to those identified in Fig. 4. These results indicate a strong association between the short-lived, rapid ozone descent events and temperature fluctuations in the tropopause region. Moreover, except for T2, all six of the other descent episodes are associated with temperature gradients exceeding 8 K km^{-1}, while T2 still exhibits a pronounced gradient of 4.2 K km^{-1}. They also represent the first detection of these descent features by the USTC Ozone Lidar, together with the first identification of their relationship to tropopause-region temperature variability using lidar-derived temperature profiles.

https://doi.org/10.5194/egusphere-2026-3261
Preprint. Discussion started: 7 July 2026

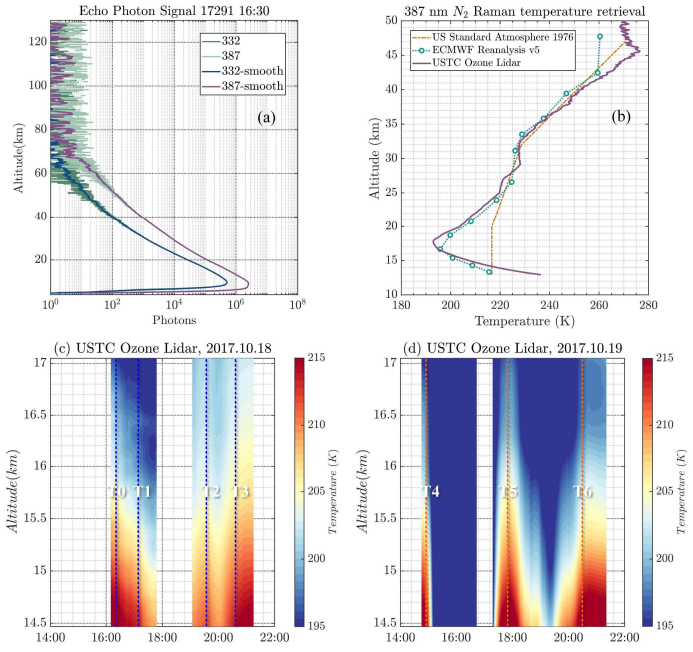

Figure 8: (a) 332 and 387nm echo optical signals received by USTC Ozone Lidar and data smoothing processing; (b) Using the USSA1976 model at a reference point of 50km, the temperature profile obtained by inversion using the 387nm vibrational Raman signal is compared with that of ERA5; (c) Temperature changes obtained from the inversion on October 18, 2017; (d) Temperature changes obtained from the inversion on October 19, 2017.

Turning back to Fig. 7(c-d), the temporal evolution of the domain-mean flux reveals pronounced stratosphere-to-troposphere transport from 08:00 to 15:00 on 18 October and from 21:00 on 18 October to 03:00 on 19 October. As the analysis here focuses on the descent event, STT is defined as positive flux. The STE signal begins to recover around 10:00 on 19 October, consistent with the features in Fig. 5a, indicating that the dominant impact of this event is confined to within roughly 24 hours. We also note that, in a domain-mean sense, the onset of the descent signal on 18 October precedes the STE timing inferred at the Yangbajing site (29°N, 99°E) from both the lidar observations and the ERA5-based diagnosis. This apparent lead suggests that the event may have first intensified in a core region away from the site, and then expanded to influence the vicinity of the observation station. It is therefore necessary to examine the spatial distribution of the mass flux to locate the main source region of the event and to analyze its dynamical drivers.

https://doi.org/10.5194/egusphere-2026-3261
Preprint. Discussion started: 7 July 2026

3.3 Spatial Distribution of Mass Fluxes Through the Tropopause

Using Wei's diagnostic framework together with ERA5 meteorological fields, we quantify the cross-tropopause mass exchange flux during 13:00-18:00 on 18 October. The flux is decomposed into contributions associated with tropopause motion, horizontal advection, and vertical motion, and we map the 6-hour mean of the instantaneous mass flux over this period (Fig.9). The red hexagon marks the location of the Yangbajing ozone lidar site. As shown in Fig.9, the horizontal transport term exhibits a spatial distribution highly consistent with that of the total flux, with a comparable magnitude. This suggests that the spatial structure of the flux during this STE event was controlled mainly by horizontal transport. However, the flux estimates shown earlier in Fig. 7(a-b) indicate that the actual downward mass transport was induced by the tropopause motion term. Moreover, Figure 9(c) further indicates that downward transport associated with the vertical transport term was also present at the Yangbajing lidar site. This behavior is consistent with the dynamical picture of tropopause folding (Sprenger et al., 2001; Škerlak et al., 2015). Specifically, a clear tropopause-folding signature is present over 25-28°N, 95-99°E within the study domain, and the folded structure can also be identified in the PV cross-section along 26°N in Fig. 7(a). Importantly, the spatial extent of the folding event closely overlaps the region of strong flux, and it accounts for the dominant contribution to the cross-tropopause mass transport during this STE episode.

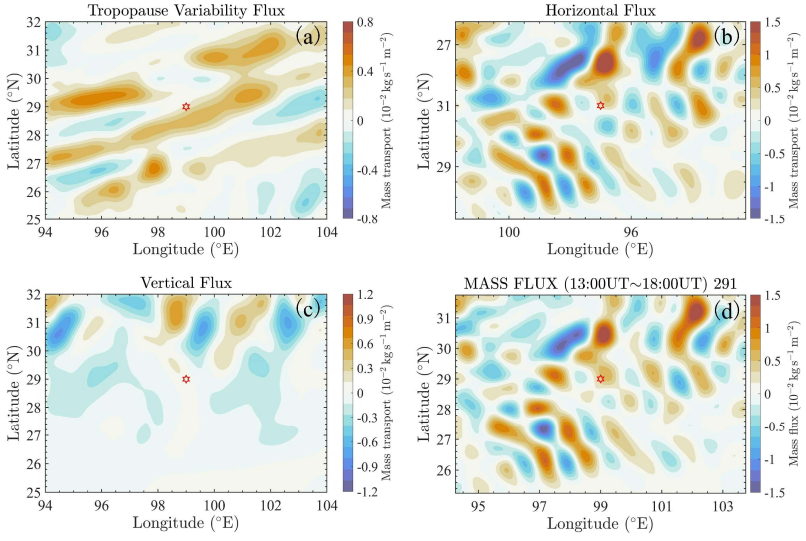

Figure 9: (a) Transport contribution from tropopause motion; (b) Horizontal transport term; (c) Vertical transport term; (d) Total cross-tropopause mass flux.

As shown in Fig. 10, we use ERA5 meteorological fields together with Wei's diagnostic to derive the spatiotemporal evolution of cross-tropopause mass flux over the study region during 18-19 October 2017. Each panel presents the 6-hour mean of the instantaneous mass flux for the corresponding interval. From Fig. 10(a-e), the tropopause-folding structure over 25-28°N, 95-

https://doi.org/10.5194/egusphere-2026-3261
Preprint. Discussion started: 7 July 2026

99°E evolves markedly with time, and the associated mass flux field exhibits pronounced temporal non-stationarity and spatial heterogeneity. This sector lies along the southeastern flank of the Tibetan Plateau, within the transition zone between the entrance and exit regions of the upper-tropospheric jet, and is therefore dynamically sensitive to frequent tropopause folding. Notably, the clearly identifiable folding band transitions from an approximately quasi-parallel, banded morphology in Fig.10(a-b) to a meridionally offset, interleaving structure in Fig. 10(g-h), suggesting a shift in the folding process from a stage modulated by near-linear wave perturbations towards a more strongly nonlinear breaking regime, possibly associated with inertial gravity waves induced by tropopause folding and their subsequent breaking. Given the fixed station location, the lidar measurements do not continuously sample the core of the tropopause fold, but more often reflect the downstream evolution and lateral modulation of the folding system (Shangguan et al., 2019; Zhang et al., 2024).

We offer the following conceptual interpretation of the dynamics. During the phase in Fig. 10(a-b), PV anomalies near the tropopause are characterized by quasi-parallel PV contours, a relatively weak meridional gradient, and limited vertical extension. This structure suggests that folding is primarily modulated by disturbances, such as planetary waves and inertial gravity waves, superimposed on the shear environment of the upper-tropospheric jet (McIntyre et al., 1983). In this stage, the lidar site (29°N, 99°E) lies on the northern flank of the folding band, within a wave-dominated sector that mainly reflects perturbations associated with tropopause undulations and PV field oscillations, while the net cross-tropopause transport remains limited. In Fig. 10(c-f), as instability strengthens in the jet-exit region, the PV gradient across the folding band sharpens markedly. An ascending branch develops on the southern side of the fold, whereas a quasi-stationary descending branch forms on the northern side near the lidar site. The site then becomes intermittently aligned with the downstream transport pathway of the PV anomaly, indicating a transition from a fold evident in morphology to one that enables effective transport (Sprenger et al., 2003). In Fig. 10(g-h), the fold exhibits clear PV tongue breakup and meridional displacement. The sawtooth-like offsets likely reflect wave breaking or nonlinear PV mixing (McIntyre et al., 1983; McIntyre et al., 1984). At this stage, ascent-descent dipoles occur more frequently on smaller spatial scales, and the vertical circulation becomes shorter-lived and more localized. The previously coherent descending conduit weakens and becomes increasingly intermittent (Stohl et al., 2003). In the vicinity of the site, this fragmented circulation and enhanced mixing reduce sustained stratosphere-to-troposphere transport (STT), manifesting as a weakened or discontinuous downward flux. In addition, the ascending branch structure to the south of the site can further interrupt the local descent pathway.

Taken together, these results indicate that the short-lived, rapid ozone descent observed during this STE event was associated not only with temperature variations, but also that the onset and recovery of the event as a whole were modulated by tropopause folding and gravity waves over the region 25-28°N, 95-99°E.

https://doi.org/10.5194/egusphere-2026-3261
Preprint. Discussion started: 7 July 2026

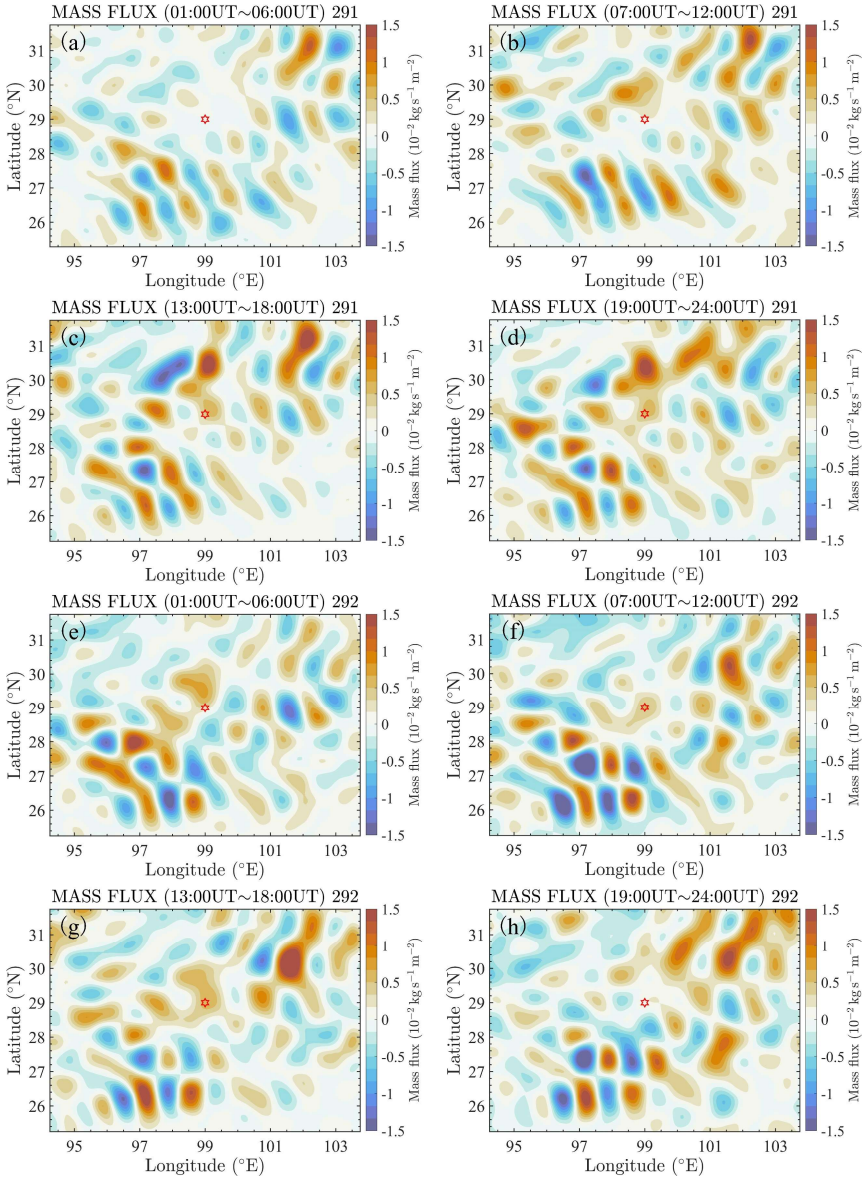

Figure 10: Spatial distribution of cross-tropopause mass flux during 18-19 October 2017.

https://doi.org/10.5194/egusphere-2026-3261
Preprint. Discussion started: 7 July 2026

3.4 Cross-tropopause ozone flux estimation based on lidar observations

Building on the mass-flux diagnostics, we further estimate the cross-tropopause ozone flux by incorporating ozone profiles from the USTC Ozone Lidar. Specifically, we use the lidar-retrieved vertical profiles of ozone number density (or concentration) to characterize ozone abundance in the troposphere and stratosphere, and thereby quantify ozone exchange fluxes across a layer extending several kilometers above and below the tropopause.

To ensure the robustness of the calculation, we assume that the ozone number densities measured at the lidar site (29°N, 99°E) are representative of the mean ozone level within 28.75-29.25°N and 98.75-99.25°E. Consistently, the mass flux is diagnosed from ERA5 gridded fields over the same spatial domain. Following the approach of Cui et al (Cui et al., 2004), we compute, from the lidar observations, the mean ozone mixing ratio within the 3 km layers immediately below and above the tropopause. By combining these layer-mean mixing ratios with the diagnosed mass flux, we obtain the net ozone flux across the tropopause at each time step. The ozone flux formulation is given by:

$$F_q = M_{up}\frac{\int_{P_{tropopause-3}}^{P_{tropopause}} q(p)dp}{\int_{P_{tropopause-3}}^{P_{tropopause}} dp} + M_{down}\frac{\int_{P_{tropopause}}^{P_{tropopause+3}} q(p)dp}{\int_{P_{tropopause}}^{P_{tropopause+3}} dp}, \quad (3)$$

In the equation, $q(p)$ represents the uniform mixing ratio of ozone at pressure p, M_{up} denotes the upward flux of substances through the tropopause, and M_{down} denotes the downward flux of substances. Positive and negative values indicate locations above and below the tropopause, respectively.

The instantaneous cross-tropopause ozone flux diagnosed at the Yangbajing lidar site for 18-19 October 2017 is shown in Fig. 10. A clear STE-related ozone descent signal is evident from 13:00 on 18 October to 12:00 on 19 October, manifested as a positive ozone flux from the stratosphere to the troposphere. In contrast, Aura satellite sampling near the site is temporally sparse. MLS typically overpasses the vicinity of Yangbajing only twice per day, whereas OMI provides at most one pass per day, which largely explains the relatively low temporal resolution of the satellite products. For 18-19 October, MLS provides three nearby footprints at (29.66°N, 98.27°E), (25.22°N, 105.20°E), and (29.66°N, 95.52°E) (red hexagons in Fig. 11). The first and third footprints are closest to the Yangbajing site, and the ozone fluxes inferred from MLS there agree well with the ERA5 estimates. By contrast, the second footprint is displaced substantially in longitude and lies outside the Tibetan Plateau, and its inferred ozone flux deviates more strongly from both the ERA5 and lidar results. Overall, the ozone flux derived from the USTC Ozone Lidar measured profiles is broadly consistent with the ERA5-driven ozone flux. More specifically, on 18 October, the lidar observations mainly capture the intensification phase and yield slightly larger diagnosed fluxes than ERA5, whereas on 19 October, during the recovery phase, the two estimates closely agree.

https://doi.org/10.5194/egusphere-2026-3261
Preprint. Discussion started: 7 July 2026

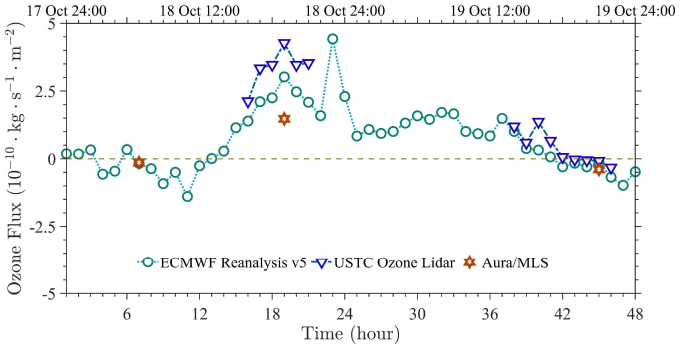

Fig. 11. Instantaneous cross-tropopause ozone flux during 18-19 October 2017.

In this study, we present an initial detection and analysis of a stratosphere–troposphere exchange (STE) event captured by ozone lidar observations. The ozone flux associated with stratosphere-to-troposphere transport derived from the USTC Ozone Lidar exhibits an instantaneous peak of approximately 3~4·10^{-10}·kg·s^{-1}·m^{-2}, slightly exceeding the corresponding estimate derived from ERA5 for the same period. Despite this difference, the overall agreement between the lidar-derived and ERA5-derived ozone fluxes supports the robustness of the flux-calculation framework. Although ozone lidar provides ozone concentration measurements with high spatial and temporal resolution, the lack of time-continuous in situ wind observations necessitates the use of ERA5 wind fields at 1-hour resolution in the flux diagnosis. Despite this limitation, our analysis demonstrates that ozone-profiling lidar can not only resolve the fine vertical structure of ozone but also, when combined with wind information, enable quantitative observation and flux estimation of STE-related downward ozone transport, thereby broadening the potential of lidar for studies of coupled atmospheric composition and dynamics.

4 Conclusion

This study uses vertical profiles of ozone density observed by our mobile differential absorption ozone lidar (USTC Ozone Lidar) located at Yangbajing, Tibet (29°N, 99°E). The system provides synchronous observations of tropospheric and stratospheric ozone over 5-50 km, offering high-spatiotemporal-resolution profile evidence for STE studies over the Tibetan Plateau. By combining 30-min signal accumulation with a moving-window procedure, the dataset maintains a high effective temporal sampling while ensuring an adequate signal-to-noise ratio and showing strong consistency with ECMWF Reanalysis v5 (ERA5) and independent satellite observations.

To corroborate the STE-related ozone descent event identified from the lidar retrievals on 18-19 October 2017, ERA5 global reanalysis was used as an independent constraint. Near the tropopause, the ozone number densities observed by the USTC Ozone Lidar agree closely with ERA5 in both magnitude and temporal evolution, lending confidence to the event identification and the subsequent quantitative diagnostics. For the rapid ozone descent features resolved by the lidar, temperature profiles

https://doi.org/10.5194/egusphere-2026-3261
Preprint. Discussion started: 7 July 2026

retrieved from the 387-nm N_2 vibrational Raman return reveal a strong correspondence with temperature fluctuations in the tropopause region. In six of the seven identified descent episodes, the associated temperature gradient exceeds 8 K km^{-1}, and even in the remaining case the gradient still reaches 4.2 K km^{-1}. These results represent the first detection of such rapid descent features by the USTC Ozone Lidar, together with the first identification of their close relationship to tropopause-region temperature variability using lidar-derived temperature profiles. In addition, the ozone descent observed at Yangbajing generally lags the broader descent over the study region (25-32°N, 94-104°E). The spatial distribution of mass flux was therefore diagnosed using the Wei formulation, and sensitivity tests of the potential-vorticity threshold indicate that 3 PVU is the most appropriate choice for this case. The diagnosed flux fields further suggest that this STE event was closely linked to tropopause folding within the study region (25-32°N, 94-104°E), with the ozone variability observed at the lidar site modulated by gravity waves associated with the evolving fold.

Building on the mass-flux diagnosis, we directly incorporate lidar-measured ozone profiles into a cross-tropopause ozone-flux framework to quantify the downward ozone flux and validate the estimates against ERA5-driven results and Aura/MLS observations. The results show that the instantaneous peak ozone flux associated with stratosphere-to-troposphere transport, measured by the USTC Ozone Lidar, is approximately $3\sim4\cdot10^{-10}\cdot kg\cdot s^{-1}\cdot m^{-2}$, slightly exceeding the corresponding ERA5-derived estimate for the same period. Because time-continuous in situ wind measurements are not available, the flux calculation still relies on ERA5 wind fields. Even with this limitation, the results demonstrate that, when combined with wind information, ozone profiling lidar can not only resolve the fine vertical structure of ozone but also provide quantitative observations and flux assessments of STE-related ozone descent. Looking ahead, we will further develop and deploy a high-accuracy, high-temporal-resolution vertical wind profiling lidar to strengthen observations of coupled composition-dynamics processes over Tibet and to extend the utility of ozone lidar in such studies.

Code and data availability

Data and code underlying the results presented in this paper are not publicly available at this time but may be obtained from the authors upon reasonable request.

Author contributions

Conceptualization, R.D. and X.F.; methodology, R.D.; validation, R.D., C.Y. and X.F.; formal analysis, C.Y.; writing-original draft preparation, R.D.; writing-review and editing, T.L.; funding acquisition, C.Y. All authors have read and agreed to the published version of the manuscript.

https://doi.org/10.5194/egusphere-2026-3261
Preprint. Discussion started: 7 July 2026

Competing interests

The authors declare no conflicts of interest

Acknowledgements

We thank all other members in team for their contribution to the system installation. The Aura/MLS data is downloaded from https://search.earthdata.nasa.gov/search.

Financial support

National Natural Science Foundation of China (42130203); National Key Research and Development Program of China (2022YFF0503703); B-type Strategic Priority Program of the Chinese Academy of Sciences (XDB41000000).

References

Baray, J. L., Courcoux, Y., Keckhut, P., Portafaix, T., Tulet, P., Cammas, J. P., ... & Delmas, R. (2013). Maïdo observatory: a new high-altitude station facility at Reunion Island (21° S, 55° E) for long-term atmospheric remote sensing and in situ measurements. Atmospheric Measurement Techniques, 6(10), 2865-2877.

Boggess, A., & Narcowich, F. J. (2009). A first course in wavelets with Fourier analysis. John Wiley & Sons.

CHEN Bin, XU Xiang-De, BIAN Jian-Chun, SHI Xiao-Hui. Irreversible stratosphere-troposphere mass exchange characteristics over the Asian summer monsoon region[J]. Chinese Journal of Geophysics (in Chinese), 2010, 53(5): 1050-1059.

Chen, C., Tian, W. S., Tian, H. Y., Huo, Y., Shu, J., Xie, F., ... & Wan, X. W. (2012). Vertical distribution of ozone and stratosphere-troposphere exchanges on the northeastern side of Tibetan Plateau. Plateau Meteorology, 31(2), 295-303.

Chen Hongbin, Bian Jianchun, Lü Daren. Advances and prospects in the study of stratosphere-troposphere exchange. Chinese Journal of Atmospheric Sciences (in Chinese), 2006, 30(5): 813-820.

Cui, H., Zhao, C., Qin, Y., Zheng, X., Zheng, Y., Chan, C. Y., & Chan, L. Y. (2004). An estimation of ozone flux in a stratosphere-troposphere exchange event. Chinese Science Bulletin, 49(2), 167-174.

Duan, A. M., & Wu, G. X. (2005). Role of the Tibetan Plateau thermal forcing in the summer climate patterns over subtropical Asia. Climate Dynamics, 24(7), 793-807.

Duchnowski, R., & Wyszkowska, P. (2025). Laser scanning data processed using Msplit estimation and sliding window algorithm. Reports on Geodesy and Geoinformatics, 120(1), 67-74.

Fang, H., & Huang, D. (2004). Lidar signal de-noising based on wavelet trimmed thresholding technique. Chinese Optics Letters, 2(1), 1-3.

https://doi.org/10.5194/egusphere-2026-3261
Preprint. Discussion started: 7 July 2026

Fang, X., Li, T., Ban, C., Wu, Z., Li, J., Li, F., ... & Tian, B. (2019). A mobile differential absorption lidar for simultaneous observations of tropospheric and stratospheric ozone over Tibet. Optics Express, 27(4), 4126-4139.

Gettelman, A., Salby, M. L., & Sassi, F. (2002). Distribution and influence of convection in the tropical tropopause region. Journal of Geophysical Research: Atmospheres, 107(D10), ACL-6.

Godin-Beekmann, S., Porteneuve, J., & Garnier, A. (2003). Systematic DIAL lidar monitoring of the stratospheric ozone vertical distribution at Observatoire de Haute-Provence (43.92 N, 5.71 E). Journal of Environmental Monitoring, 5(1), 57-67.

Hansen, G., Bramstedt, K., Rozanov, V., Weber, M., & Burrows, J. P. (2003, August). Validation of GOME ozone profiles by means of the ALOMAR ozone lidar. In Annales Geophysicae, 21(8), 1879-1886. Göttingen, Germany: Copernicus Publications.

Holton, J. R., Haynes, P. H., McIntyre, M. E., Douglass, A. R., Rood, R. B., & Pfister, L. (1995). Stratosphere-troposphere exchange. Reviews of Geophysics, 33(4), 403-439.

Kovalev, V. A., & Eichinger, W. E. (2004). Elastic lidar: theory, practice, and analysis methods. John Wiley & Sons.

Lelieveld, J., & Dentener, F. J. (2000). What controls tropospheric ozone? Journal of Geophysical Research: Atmospheres, 105(D3), 3531-3551.

McDermid, I. S., Haner, D. A., Kleiman, M. M., Walsh, T. D., & White, M. L. (1991). Differential absorption lidar systems for tropospheric and stratospheric ozone measurements. Optical Engineering, 30(1), 22-30.

McIntyre, M. E., & Palmer, T. N. (1983). Breaking planetary waves in the stratosphere. Nature, 305(5935), 593-600.

McIntyre, M. E., & Palmer, T. N. (1984). The “surf zone” in the stratosphere. Journal of Atmospheric and Terrestrial Physics, 46(9), 825-849.

Randel, W. J., & Park, M. (2006). Deep convective influence on the Asian summer monsoon anticyclone and associated tracer variability observed with Atmospheric Infrared Sounder (AIRS). Journal of Geophysical Research: Atmospheres, 111(D12).

Randel, W. J., Park, M., Emmons, L., Kinnison, D., Bernath, P., Walker, K. A., ... & Pumphrey, H. (2010). Asian monsoon transport of pollution to the stratosphere. Science, 328(5978), 611-613.

Reiter, E. R. (1975). Stratospheric-tropospheric exchange processes. Reviews of Geophysics, 13(4), 459-474.

Shangguan, M., Wang, W., & Jin, S. (2019). Variability of temperature and ozone in the upper troposphere and lower stratosphere from multi-satellite observations and reanalysis data. Atmospheric Chemistry and Physics, 19(10), 6659-6679.

Škerlak, B., Sprenger, M., Pfahl, S., Tyrlis, E., & Wernli, H. (2015). Tropopause folds in ERA-Interim: Global climatology and relation to extreme weather events. Journal of Geophysical Research: Atmospheres, 120(10), 4860-4877.

Sprenger, M., Croci Maspoli, M., & Wernli, H. (2003). Tropopause folds and cross-tropopause exchange: A global investigation based upon ECMWF analyses for the time period March 2000 to February 2001. Journal of Geophysical Research: Atmospheres, 108(D12).

Stohl, A., Bonasoni, P., Cristofanelli, P., Collins, W., Feichter, J., Frank, A., ... & Zerefos, C. (2003). Stratosphere-troposphere exchange: A review, and what we have learned from STACCATO. Journal of Geophysical Research: Atmospheres, 108(D12).

https://doi.org/10.5194/egusphere-2026-3261
Preprint. Discussion started: 7 July 2026

Tian, W., Chipperfield, M., & Huang, Q. (2008). Effects of the Tibetan Plateau on total column ozone distribution. Tellus B: Chemical and Physical Meteorology, 60(4), 622-635.

Wei, M. Y. (1987). A new formulation of the exchange of mass and trace constituents between the stratosphere and troposphere. Journal of Atmospheric Sciences, 44(20), 3079-3086.

Weitkamp, C. (2005). Lidar: range-resolved optical remote sensing of the atmosphere. Vol. 102. Springer Science & Business Media.

Wirth, V., & Egger, J. (1999). Diagnosing extratropical synoptic-scale stratosphere-troposphere exchange: A case study. Quarterly Journal of the Royal Meteorological Society, 125(554), 635-655.

Yang Jian, Lv Daren. A Simulation Study of Stratosphere-Troposphere Exchange due to Cut-off-low over Eastern Asia. Chinese Journal of Atmospheric Sciences (in Chinese), 2003, 27(6): 1031-1044.

YANG Jian, LU Da-Ren. Diagnosed Seasonal Variation of Stratosphere-Troposphere Exchange in the Northern Hemisphere by 2000 Data. Chinese Journal of Atmospheric Sciences (in Chinese), 2004, 28(2): 294-300.

Yin, S., & Wang, W. (2006). Denoising lidar signal by combining wavelet improved threshold with wavelet domain spatial filtering. Chinese Optics Letters, 4(12), 694-696.

Zhang, M., Tian, W., Chen, L., & Lü, D. (2010). Cross-tropopause mass exchange associated with a tropopause fold event over the northeastern Tibetan Plateau. Advances in Atmospheric Sciences, 27(6), 1344-1360.

Zhang, Y., Huang, Q., Guo, K., Wang, M., Liao, H., Chou, Y., & He, X. (2024). Tropopause folds over the Tibetan Plateau and their impact on water vapor in the upper troposphere-lower stratosphere. Climate Dynamics, 62(2), 1423-1437.

Zhou, S., & Zhang, R. (2005). Decadal variations of temperature and geopotential height over the Tibetan Plateau and their relations with Tibet ozone depletion. Geophysical Research Letters, 32(18).